Recyclable and Self-Healing Stretchable Strain Sensor Based on Liquid Metal and Diels–Alder Polymer for Smart Wearable Applications

Rathul Nengminza Sangma, Seppe Terryn, Maximilian Krack, Kevin Langlois, Fatemeh Sahraeeazartamar, Ehsan Mirabdollah, Lennert Purnal, Parth Vinayakrao Sewlikar, Iris De Graeve, Michael Daenen, Joost Brancart, Guy Van Assche, Wim Deferme, and Bram Vanderborght

***Abstract*—The vulnerability of smart wearables necessitates stretchable sensors capable of recovering their functionality after sustaining damage. Recent research on liquid metal (LM)-based sensors demonstrates the potential of these highly stretchable, conductive, and reliable sensors. Unlike previous studies using silicone-based substrates, this article proposes a self-healing (SH), biocompatible strain sensor based on Galinstan embedded in a Diels–Alder (DA) polymer encapsulant. The novelty of this sensor lies in its ability to restore sensing and mechanical functionalities through numerous damage-healing cycles. This research outlines the fabrication and quasi-static and dynamic characterization of the strain sensor, enabling analysis of its strength, sensitivity, hysteresis, response time, drift, and healing performance. Healing is investigated by repeatedly rupturing the sensor in half, then healing it at 60 °C for 4 h before recharacterization. On a mechanical level, healing efficiencies of 80% are achieved based on recovered strain, while on a sensor level, the gauge factor (GF) is recovered with 105% efficiency. The degree of hysteresis (DH) for resistance–strain is less than 1%, and the sensing behavior is independent of strain rate. The sensor has a response time of 220 ms with an acceptable drift of 5% over 800 cycles. This article demonstrates the feasibility of recycling the sensor by outlining a method to separate the substrate from the LM and reprocess it. In addition, the sensitivity and biocompatibility of both pristine and healed sensors are validated through case studies, such as tracking finger and knee joint angle bending, highlighting their potential for smart wearable applications. Supplementary video material can be found at https://www.youtube.com/watch?v=SeLYJ6_qT_k**

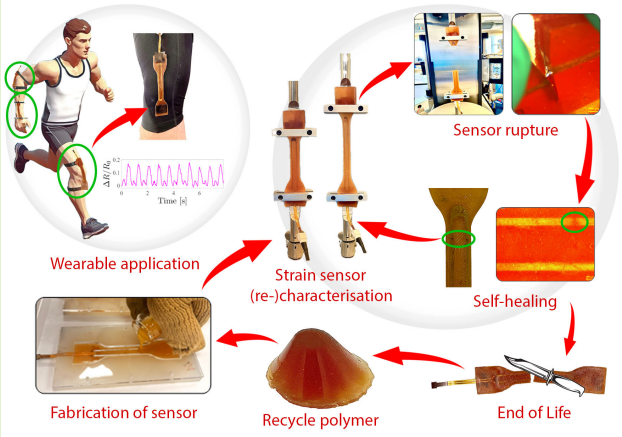

***Index Terms*— Human motion monitoring, liquid metal (LM), recyclable strain sensor, self-healing (SH) polymers, strain gauge, wearable robotic applications.**

I. Introduction

IN THE domain of wearable robotics, the demand for stretchable and sustainable electronics continues to rise steadily [1], [2], [3], [4], [5]. Flexible electronics are notable for their low stiffness, high deformability, and stretchability [6], [7], [8], [9], [10]. These properties make flexible and stretchable electronics suitable for applications, such as wearable medical devices [11], flexible displays [12], soft robotics [13], smart/electronic skins [14], and stretchable pressure and strain sensors [2], [15]. However, a key challenge for flexible electronics remains their susceptibility to damage [16], which limits their lifespan and undermines their economic competitiveness and sustainability. Nevertheless, in the aforementioned applications, sustainability is crucial, as environmental protection remains a significant concern [17], [18]. Therefore, advancements in materials for both the substrate and the conductive circuit will be crucial to ensuring the widespread, sustainable adoption of flexible and stretchable electronics in the future [18], [19]. State-of-the-art stretch-

Received 20 May 2025; accepted 4 July 2025. Date of publication 16 July 2025; date of current version 15 August 2025. This work was supported by the Research Foundation—Flanders [Fonds Wetenschappelijk Onderzoek (FWO)] through the Strategisch BasisOnderzoek (SBO) Project under Grant S007423N. The work of Seppe Terryn was supported by FWO under Grant 1100416N. The work of Maximilian Krack was supported by FWO under Grant 1SH1C24N. The work of Kevin Langlois was supported by FWO under Grant 1258523N. The associate editor coordinating the review of this article and approving it for publication was Dr. Jitendra Singh. *(Corresponding author: Rathul Nengminza Sangma.)*

Please see the Acknowledgment section of this article for the author affiliations.

Digital Object Identifier 10.1109/JSEN.2025.3588043

able sensors can be categorized into two types: those with intrinsically conductive substrates, where the substrate itself is conductive, and those with nonintrinsically conductive substrates that incorporate embedded conductive materials for sensing. This research focuses on the latter—nonintrinsically conductive substrates.

A. Self-Healing (SH) Substrate via Diels–Alder (DA) Polymers

In the state-of-the-art liquid metal (LM)-based stretchable sensors, the substrates encompass a range of materials, including bioderived substances and silicone rubbers [2], [20]. Silicone-based materials, such as EcoFlex, Sylgard, Elastosil, and DragonSkin, are commonly used due to their high stretchability, mechanical strength, and low cost [21]. However, these materials lack SH capabilities, as they cannot recover functionality after damage. This damage can occur when the sensor is torn or ruptured from overstretching, cut by a sharp object, or when fatigue (e.g., microcracks) leads to damage propagation and failure. This limitation impacts the sustainability and reliability of stretchable sensors and the devices in which they are integrated, including smart, soft wearables, and soft robots [22]. Delamination is another issue that undermines the robustness of stretchable sensors, which are typically produced through multistage molding. Weak interfacial strength at manufacturing interfaces, which typically rely on weak secondary interactions (e.g., adhesion), detaches over time due to stress concentrations, leading to performance degradation [22].

Endowing stretchable sensors with SH capabilities leads to prolonged device lifetimes, enhanced reliability, sustainability, easier maintenance, and reduced material consumption for producing new devices. In this article, an SH polymer based on thermoreversible DA crosslinks is proposed as the material for producing the substrate. Akin to traditional silicone-based materials, this DA polymer offers shock absorption and impact protection, with the added benefit of having SH capability [22]. The DA polymer network is formed by the reversible cycloaddition reaction between a conjugated diene (here furan) and a dienophile (here maleimide), which forms reversible DA crosslinks [23]. The resulting DA polymers benefit from extensive tunability in their mechanical [24] and electrical properties [25], [26], making them suitable for designing flexible substrates with versatile characteristics. Their intrinsic SH capability is based on DA crosslinks and is restored after healing. In other words, these DA polymers can undergo multiple damage-healing cycles [27]. Upon damage, the DA crosslinks in the network mechanically break, creating reactive bismaleimide and furan. Being an equilibrium reaction, these reactive components rebind upon recontact, thus healing the damage and recovering the initial material properties, as shown in Fig. 1. This process can be accelerated by heating (e.g., to 60 °C), which increases the rate of the DA reaction. In principle, this healing process can be repeated indefinitely, allowing for multiple damage-healing cycles without significant degradation of the material. In addition, the relatively high bond energy of DA bonds, compared to other reversible bonds including hydrogen bonds, ensures that these SH polymers have good mechanical properties (strength, elastic recovery, and creep resistance), in combination with room- or moderate-temperature healing [28].

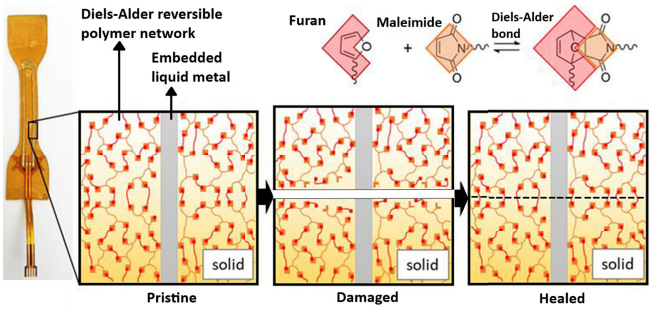

Fig. 1. Schematic of the SH sensor/circuit. The encapsulant is a reversible polymer network with DA crosslinks. Upon damage, the bonds and LM channel break; during healing (assisted by heat), the bonds reform and conductivity is restored.

In addition to SH, DA polymers mitigate delamination issues in assembled parts by forming strong interfaces through reversible bonding, e.g., DA covalent bonds, which can be achieved with a heat-cool posttreatment [29], [30]. This is also true when chemically binding and joining two DA polymers with different mechanical properties, achieved by varying their DA crosslink density [24]. Consequently, DA polymers have been utilized to fabricate durable multimaterial soft robots with robust interfaces, employing traditional casting methods [30]. When DA polymers are heated above their degelation temperature (the temperature at which the polymer network dissociates into its liquid phase), the liquid polymer can be reprocessed and reshaped using various additive and formative manufacturing techniques [6], [22]. Most of their thermoreversible crosslinks break, causing their networks to degel into a viscous liquid. This reprocessing ability offers significant potential for the creation of recyclable soft devices, including wearable technology and soft robotics.

B. Embedded SH Sensor via LM

Piezoresistive SH sensors can be achieved by providing the substrate material with intrinsic electrical conductivity by compounding it with fillers such as graphene [31] or carbon black. Although studies [25] have shown that this can lead to DA compounds that combine SH with piezoresistive sensing, they also show that this approach leads to highly nonlinear, time-dependent (e.g., hysteresis) sensors that are challenging to model and calibrate [15]. Although machine learning techniques can provide a system-level solution [32], they require extensive sampling and training. Furthermore, SH efficiency is limited, as even though piezoresistive sensing is restored after healing, extensive recalibration of the analytical [15] or machine learning model [32] is necessary. Hence, these challenges have led to material-level research to develop improved SH stretchable strain sensors based on LMs.

LMs are popular for stretchable sensors because they combine electrical conductivity in a liquid and stretchable state [2], [5], [7], [8], [33], [34], [35]. Many of these metals, including gallium alloys such as Galinstan (an alloy of gallium, indium,

and tin) are nontoxic and biocompatible. Being liquid, these LMs inherently possess an SH property and provide great opportunities for creating SH stretchable sensors. This research uses Galinstan as a conductive material. Galinstan exhibits high surface tension and shares similarities with mercury, such as high boiling point and conductivity, but is safer due to its low toxicity and low vapor pressure [5], [36]. Although Galinstan can oxidize upon exposure to oxygen, the oxide layer acts as a protective barrier [37]. Its sensing performance remains stable for extended periods [38]. In conclusion, Galinstan is ideal for developing circuit-based SH sensors in wearable applications due to its less toxic behavior, biocompatibility, low melting point, and negligible vapor pressure [36], [39].

This study introduces a novel SH stretchable sensor by combining the benefits of stretchable DA polymer with those of conductive Galinstan for several healed cycles without delamination issues. Galinstan is incorporated as a circuit within a DA substrate. The innovation lies in the sensor's ability to recover both electrical and mechanical functionalities after multiple damage cycles, maintaining performance comparable to its original state and thereby extending the sensor's lifespan. Moreover, the substrate can be reprocessed at the end of its lifespan, further enhancing the sensor's ecological sustainability. Experimental characterization will demonstrate that combining Galinstan with the DA substrate yields a fully SH sensor. This sensor is well-suited for wearable robotics, thanks to its rapid elastic recovery and minimal hysteresis, compared with other SH strain sensors in the state of the art [40]. This article details the materials, design, fabrication, characterization, modeling, recalibration, recycling, and validation processes for motion tracking for smart wearables. In terms of characterization, the sensors undergo quasi-static and dynamic electromechanical testing, enabling analysis of the sensor's strength, sensitivity, hysteresis, step response time, drift, and SH performance.

II. Materials and Methods

A. Materials

The stretchable strain sensor is composed of Galinstan, DA polymer noted as DPBM-FT5000-r0.5 [28], and a flexible PCB which facilitates a reliable electrical connection between the data acquisition system (DAQ) and the LM. The reagents needed to synthesize the DA polymer are shown in Fig. 2(a)–(d). Furfuryl glycidyl ether (FGE) was obtained from BLD Pharmatech GmbH, Germany. Jeffamine JT5000 with an average molecular weight of 5709 g/mol ($R = 0$, $n = 0$ and $x + y + z = 96.8$), was provided by Huntsman. 1,1′-(methylenedi-4,1-phenylene) bismaleimide (DPBM, 95%) and 4-tert-butylcatechol were purchased from Sigma-Aldrich. All chemicals were used as received. Galinstan LM was ordered from [41], an eutectic alloy of 60–65 wt.% gallium, 20–25 wt.% indium, and 5–10 wt.% tin. It possesses high electrical conductivity (2.3×10^6 S/m) and a low melting point (−19 °C). Fig. 2(h) shows a drop of Galinstan with high cohesive force and significant surface tension, resulting in an obtuse contact angle on a flat surface.

1) Synthesis of DA Polymer Encapsulant: The synthesis of the DA substrate, DPBM-FT5000-r0.5, is conducted in two steps. Initially, Jeffamine JT5000 is reacted with furan moieties via an irreversible epoxy-amine reaction with monofunctional FGE without the use of solvent or catalyst. This first reaction is carried out under stoichiometric conditions (((amine NH)/epoxy) = 1) in an oil bath at 60 °C, stirred for 5 days, followed by heating to 90 °C for two additional days to ensure completion of the reaction. It yields a furan functionalized Jeffamine, noted as FT5000. In the second step, the bismaleimide crosslinker, DPBM powder, was dry mixed with powder of 4-tert-butylcatechol (1 wt.%), a radical inhibitor. This mixture was melted at 160 °C and then mixed with FT5000, which was also preheated to 160 °C. In this mixing process, a maleimide-to-furan ratio (r) of 0.5 was chosen. The mixture was stirred for 1 min and then poured directly into a Teflon mold. Subsequently, the polymer was allowed to cure for 24 h, during which the DA reaction between the maleimide and furan formed a polymer network via cross linking. For additional synthesis details, please refer to the publication [24], [28].

2) Flexible PCB and Stencil: Creating reliable connections between LM circuits in stretchable electronics and external electronics, such as DAQ systems, is generally challenging. In this study, to ensure reliable connections between Galinstan and DAQ, a custom-designed flexible PCB was employed, as depicted in Fig. 2(j) [42]. The flexible PCB consists of a thin copper strip sandwiched between flexible polyimide layers, featuring four electroless nickel immersion gold-coated copper bond pads for a four-wire connection. Two design features are implemented to enhance reliability during stretching: 1) the inclusion of four "fingers" that extend into the device to strain isolate the transition area and 2) vertical interconnect access holes that promote mechanical interlocking between the substrate layers. A reusable stainless steel stencil with a thickness of 120 μm was used that formed a path of 60-mm long and 1-mm wide, as shown in Fig. 2(f). A U-shaped circuit was used during sensor fabrication composed of LM for sensing. The total electrical path is 120-mm long with an enlarged U-junction to reduce cross-sensitivity.

B. Methods

1) Sensor Design: The design of the stretchable strain sensor is based on the standard dumbbell shape of ASTM-D412-C, as shown in Fig. 2(e) and has a thickness of 3 mm. The width was increased from 6 to 11 mm to provide ample space to accommodate the LM circuit and reduce the risk of short-circuiting in case of rupture. This allows for the use of a U-shaped circuit with a 7-mm spacing between the LM channels, ensuring adequate separation to minimize short-circuit risks. Moreover, a wider sensor increases the cross-sectional area, giving it a larger "SH surface." This makes it easier for the material to reconnect and repair itself after damage, helping to restore the sensor's mechanical strength. The LM channels have a width of 1 mm and an average height of 35 μm.

2) Sensor Fabrication: The sensor manufacturing process focuses on the reprocessability and high interfacial strength of the DA polymer to minimize delamination issues and is shown in Fig. 3. It involves 12 steps, including casting a first

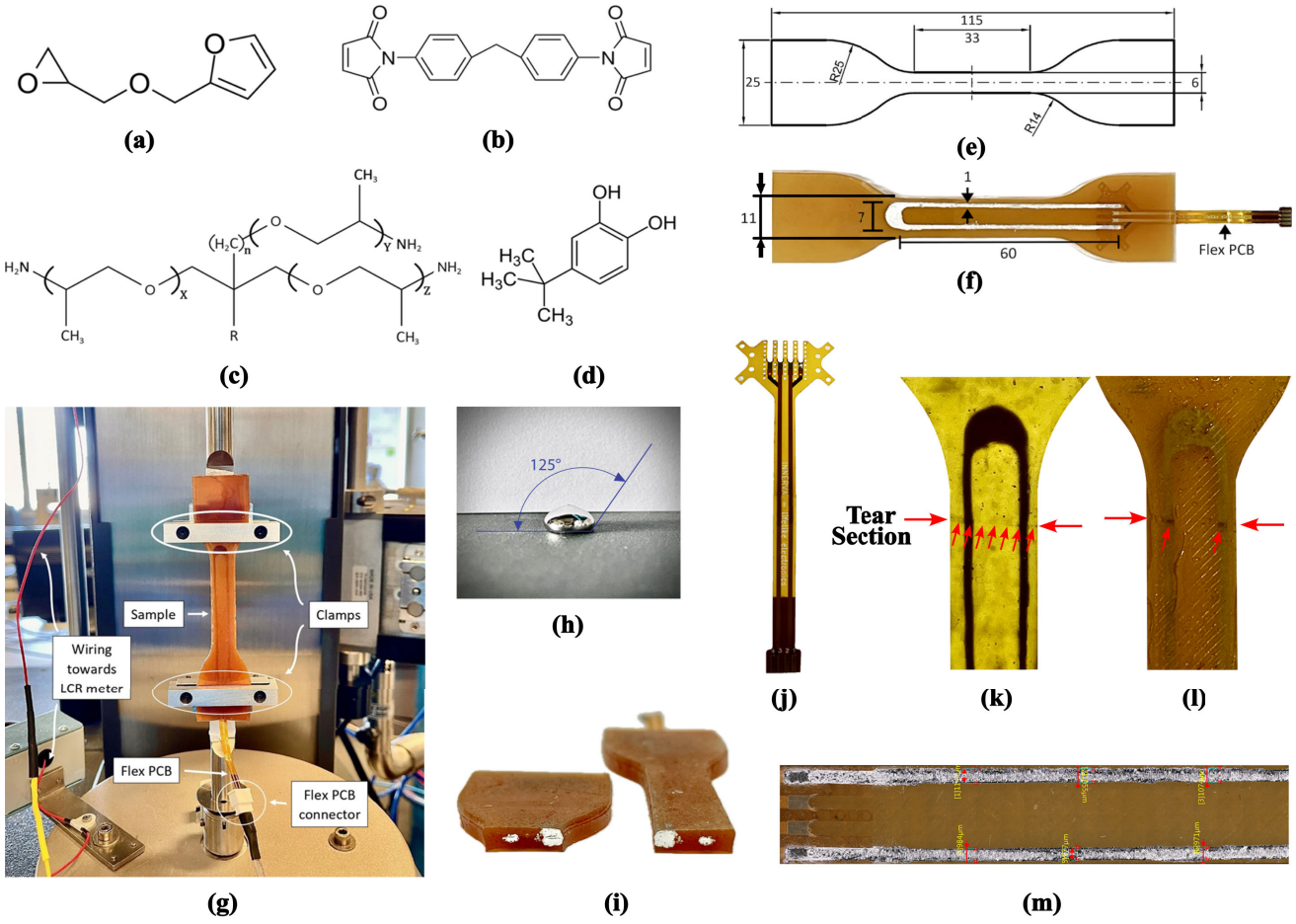

Fig. 2. Illustration of the chemical structures of key reagents used for making the DA polymer substrate. (a) FGE. (b) DPBM (1,1′-(Methylenedi-4,1-phenylene) Bismaleimide. (c) Jeffamine T5000 with $x+y+z=96.8$ and $n=0$. (d) 4-tert-butylcatechol used as a radical inhibitor. (e) Schematic of the dogbone-shaped specimen following ASTM D412-C standards used for making the sensor. (f) Fabricated sensor sample adapted from the standard by increasing the width of the substrate from 6 to 11 mm with a thickness of 3 mm. All dimensions in the image are in millimeters. (g) Experimental setup was used for tensile testing, showing the strain sensor clamped in the TA RSA-G2 instrument with electrical connections from the flexible PCB to the LCR meter for resistance measurement. (h) Image of a nontoxic and biocompatible Galinstan droplet exhibiting strong cohesive and surface tension properties, forming an obtuse contact angle on a flat surface. (i) Image of the strain sensor ruptured across the cross section after sixth rupture-healing cycle. Silver-colored Galinstan can be seen protruding from its trace through the ruptured cross section. (j) Top view of a thin and flat flexible PCB featuring four gold-plated copper bond pads at each end for electrical connection between Galinstan and the DAQ system. (k) and (l) Healed strain sensor after cross-sectional rupture is seen from top view. The tear section in (k) is indicated with arrows, with the light source illuminating from the bottom of the sensor. The silvery Galinstan trace in (l) can be seen turning black at the spot during the cross-sectional rupture. This indicates that the LM has oxidized at the spot due to exposure to oxygen in the open air. (m) Image of a silvery Galinstan trace sprayed on an SH substrate, viewed through an optical microscope. The width of the Galinstan trace is on average 1-mm wide and 60-mm long.

layer of DA polymer, depositing the LM onto this first layer, and covering it with a second layer of DA polymer through overcasting and postcuring.

First, a negative mold was 3-D printed using PLA material in UltiMaker S5. Next, "Dragon Skin[1] 20," a silicone rubber provided by Smooth-On Inc., was cast into the negative mold and cured for four hours at room temperature. Subsequently, the part was demoulded and used as a mold to produce the sensor. In this Dragon Skin mold, the liquid DPBM-FT5000-r0.5 was cast (see the last stage of synthesis in Section II-A1). The result was a first layer of the dogbone substrate with a thickness of 1.5 mm. The LM circuit was then deposited on this initial layer. This involved aligning and placing the flexible PCB connector onto the substrate, followed by positioning a metal stencil on top of the substrate and PCB. This stainless steel stencil featured a U-shaped cutout. Then, Galinstan was deposited using an in-house automated spray coater, consisting of a 3-D printer with a motorized syringe, a 3-D-printed spray nozzle, and a pressure valve. Specifically, Galinstan was sprayed from a height of 10 cm with a flow rate of 1 mL/min, a pressure of 3.5 bar, and a nozzle speed of 25 mm/s, as shown in Fig. 3 (Step 7). Once the stencil was removed, a U-shaped Galinstan channel remained on top of the DA substrate. This channel was form-stable due to a combination of surface tension and an oxide layer, and it was directly in contact with the flexible PCB connector. In the following step, a second layer of liquid DA polymer with a thickness of 1.5 mm was cast on top of the circuit, which remained in shape during

[1]Trademarked.

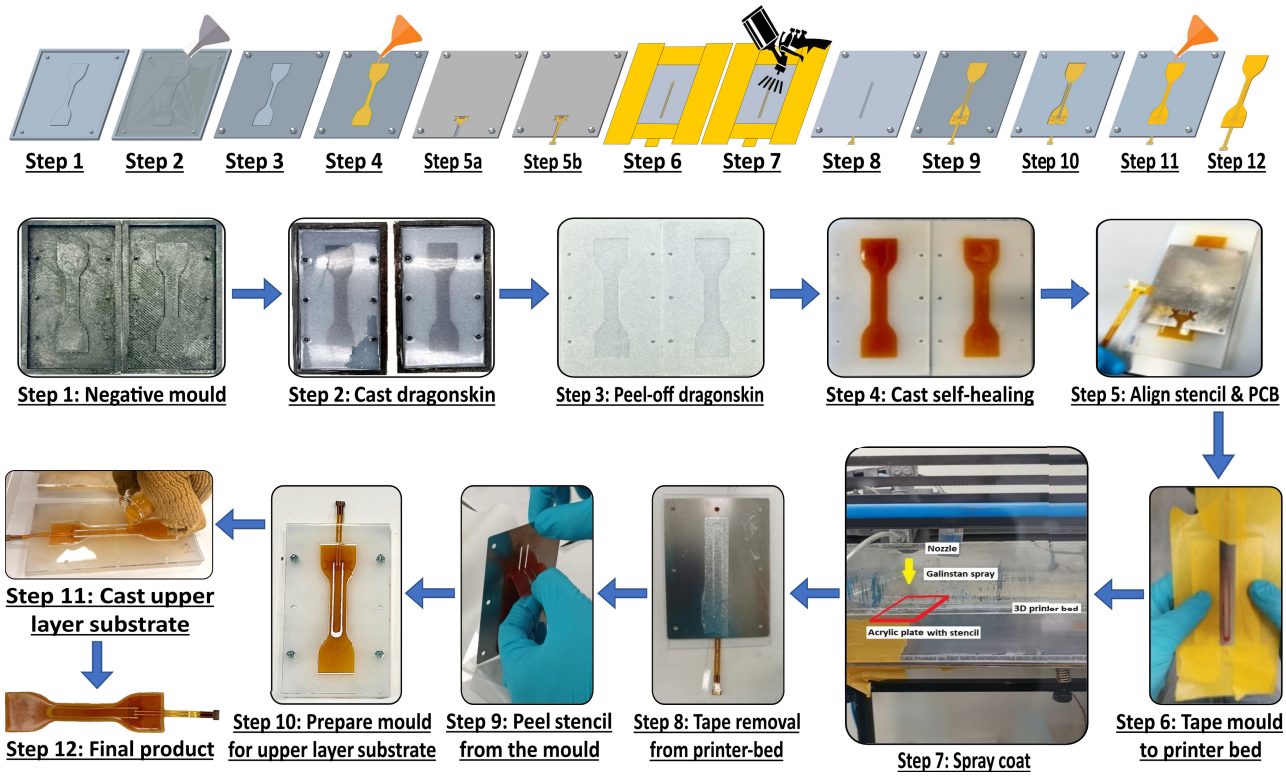

Fig. 3. Fabrication process of the SH and recyclable stretchable strain sensor. (Step 1) Print a 3-D negative mold using PLA material, in preparation for casting a positive mold. (Step 2) Cast a positive mold using "Dragon Skin 20" material onto the negative mold, followed by a 4-h curing period. (Step 3) Remove the positive "Dragon Skin 20" mold from the negative mold, ready for casting the SH material on it. (Step 4) Cast the SH DPBM FT-5000-r0.5 material onto the positive mold, forming the first-layer substrate with a thickness of 1.5 mm. (Step 5) Align the metal stencil to position the flexible PCB onto the SH substrate. Precisely place the flex PCB onto the SH material surface while maintaining alignment. (Step 6) Replace the stencil used for aligning the flexible PCB with a metal stencil featuring a "U"-shaped cut-out for the spraying process. Tape the mold with the stencil on the bottom of the printer bed for spraying LM. (Step 7) Spray Galinstan using the printer and guided automated path, producing an LM trace with a certain thickness. (Step 8) Remove the mold from the printer bed by detaching the tapes. (Step 9) Peel the metal stencil from the polymer substrate and the mold, exposing a "U"-shaped trace of Galinstan on the SH material. (Step 10) Overlay a 1.5-mm-thick Plexiglas piece, cut in a dogbone shape, to cast the second layer of SH material. (Step 11) Pour the second layer of SH material on the mold supported by the Plexiglas and let it cure for 24 h. (Step 12) Remove the SH substrate from the Plexiglas and mold, ready for strain sensing.

the process. Next, this layer was cured at room temperature for 24 h, after which the sensor was removed from the mold. In the last postprocessing step, the sensor was placed in an oven at 60 °C for 2 h to minimize delamination issues and ensure interfacial bonding between the two DA layers. This results in high interfacial strength, providing robustness and hermetic sealing of the Galinstan channel.

3) Electromechanical Characterization: Quasi-static and dynamic analysis are performed on a dynamic mechanical analyzer (DMA), RSA-G2 of TA Instruments [see Fig. 2(g)], equipped with a Keysight E4980AL LCR meter, to measure the impedance during mechanical analysis. All tests were performed using alternating current (ac), with an amplitude of 5 V and a frequency of 1 kHz. All tests were done at room temperature, fluctuating between 20 °C and 25 °C.

4) Damage and SH Cycle: To push the SH to its limits, the stretchable strain sensor was cut completely in half using a scalpel blade. Next, the fracture surfaces were recombined and recontacted manually, minimizing misalignment using visual inspection. The sensor was then healed by placing it back in the dogbone-shaped silicone mold and in an oven at 60 °C for 4 h. Although healing could be achieved at room temperature [28], using a slightly elevated temperature accelerated the process and provided control, which is useful when the system is misaligned, contaminated, or requires manual intervention. Room-temperature healing of DA polymer DPBM-FT5000-r0.5 has been demonstrated by Safaei et al. [28], where it is shown that full restoration of mechanical properties can occur within a few hours, with partial healing occurring within minutes after recontacting the damaged surfaces. In addition, Legrand et al. [43] reported successful healing at moderate temperatures (e.g., 45 °C), further confirming the material's potential for low-temperature or autonomous healing. In our case, the same DA polymer chemistry was used, with the only modification being the embedded LM, which may chemically interfere with the DA healing mechanism to some extent at the interface but does not affect the overall healing kinetics. Therefore, similar room-temperature healing behavior is expected, and the use of 60 °C in this study was chosen purely to reduce the healing time.

5) SH Assessment: A widely used method for evaluating the SH capability of materials and the electrical/sensing performance of sensors is the calculation of *healing efficiency*

(η_P), which quantifies the extent to which a property recovers after healing [28], [44]. It is mathematically defined as follows:

$$\eta_P = \frac{P_{n\text{th healed state}} - P_{n\text{th damage state}}}{P_{\text{pristine state}} - P_{n\text{th damage state}}} \tag{1}$$

where "P" represents a material property such as Young's modulus (E), fracture strain (ϵ), fracture stress (σ), or toughness. In addition, "P" can denote electrical/sensor performance parameters like conductance and gauge factor (GF).

In this study, the sensor undergoes *severe damage* by being completely ruptured during testing, reducing all measured properties to 0 in the damaged state. This simplifies (1) to

$$\eta_P = \frac{P_{n\text{th healed state}}}{P_{\text{pristine state}}}. \tag{2}$$

Here, the healing efficiency of a given property represents the ratio of a healing state to its initial pristine state, with 100% efficiency indicating full recovery.

Mechanical properties such as Young's modulus (E) and toughness are determined using

$$E = \frac{\sigma}{\epsilon}, \quad \text{Toughness} = \int_0^{\epsilon_{\text{fracture}}} \sigma \, d\epsilon \tag{3}$$

where σ represents stress and ϵ represents strain. Young's modulus quantifies the stiffness of the material, while toughness represents the energy absorbed before fracture, which is crucial for evaluating structural resilience after healing.

Strain at fracture ($\epsilon_{\text{fracture}}$) and stress at fracture (σ_{fracture}) are key parameters in assessing a material's mechanical failure point. Strain at fracture ($\epsilon_{\text{fracture}}$) quantifies how much a material deforms before breaking, with higher values indicating greater ductility. Stress at fracture (σ_{fracture}) measures the maximum stress a material can withstand before breaking, indicating its load-bearing capacity.

These parameters indicate whether the material regains its original mechanical integrity after healing. If their postheal-ing values approach the pristine state, the material exhibits effective mechanical recovery.

To assess the restoration of electrical/sensing performance, the GF is used as a key parameter. It is defined as follows:

$$\text{GF} = \frac{\Delta R/R_0}{\epsilon} \tag{4}$$

where $\Delta R = R - R_0$ is the change in resistance and ϵ is the applied strain. The GF represents the ratio of the change in relative resistance to the applied strain, indicating how effectively the sensor transduces mechanical deformation into an electrical signal [45]. A higher GF implies a more sensitive strain sensor. Conductance, the reciprocal of resistance, represents the ease with which the electrical current flows through the sensor and is measured initially before the experiment begins.

By analyzing these parameters, the extent of recovery in both mechanical properties and strain sensing performance is determined, providing a comprehensive understanding of the sensor's SH capability.

III. Results and Discussion

A. Sensing and SH Performance

As an initial assessment of the SH capability of the stretchable strain sensor, both the pristine and healed sensors (Section II-B4) were subjected to a quasi-static tensile test with a strain ramp of 0.25%/s until rupture, while their impedance was tracked (Section II-B3). First, it can be seen that the pristine sensor can reach strains up to 50% before fracture, providing a wide strain window of operation for smart wearable applications. The conductance of the pristine sensor at rest was 0.36 S, corresponding to a resistance of 2.8 Ω. This demonstrates the high conductivity of the embedded Galinstan circuit within the DA polymer. Such high conductivity enables LM circuits to function as a signal transmission pathway, establishing SH and stretchable connections in stretchable sensors with significantly lower resistances [15] and external electronics, e.g., DAQs. In addition, its GF was calculated at the 15% strain, which is 2.08, allowing for accurate detection of small changes in strain. Although this value aligns with the typical GFs reported in the literature for elastomeric sensors (typically 10^0–10^2) [46], the sensor's GF can be further improved by reducing the width of the LM circuit. Sensor sensitivity can be improved by increasing the number of loops in a planar design or by incorporating multiple stacked layers in a 3-D configuration.

The sensor was subjected to a damage and consecutive healing cycles six times during the tensile testing procedure. The visual inspection confirmed that fractures occurred consistently in the same cross-sectional area each time. Fig. 4(a) and (b) displayed the stress versus strain relationship and the change in relative resistance versus strain relationship, respectively, for both the pristine and healed sensors. Based on this experimental data, Young's modulus (E) was calculated via linear regression in the 0%–1% strain window. The fracture stress and strain were calculated as the final values of stress and strain before rupture, while the toughness was measured as the stress integral in the 0 to fracture strain window. Based on these parameters and the sensor's conductance at rest, the healing efficiencies were calculated and presented in Fig. 4(c).

On a mechanical level, the trends in Fig. 4(c) shows that Young's modulus slightly increases with every damage-healing cycle. One possible explanation for the stiffening of the material upon straining it to 50% is that the crosslink density slightly increases with each damage-healing cycle [23]. Extending the annealing time after sensor fabrication could eliminate these variations; however, this should be investigated in a follow-up study. Nevertheless, by looking at the results of the first damage-healing cycle, it can be concluded that the healing is quite successful, illustrated by an 87% and 80% healing efficiency based on the fracture stress and fracture strain, respectively. Aside from this, it is clear that with every damage-healing cycle, the sensor's strength represented by its fracture stress, fracture strain, and toughness reduces [see Fig. 4(c)]. This decrease can be explained by the fact that when the sensor is cut, part of the cross-sectional fracture surfaces can be contaminated by LM (oxide). This results in a loss of "SH surface," hence a loss in strength.

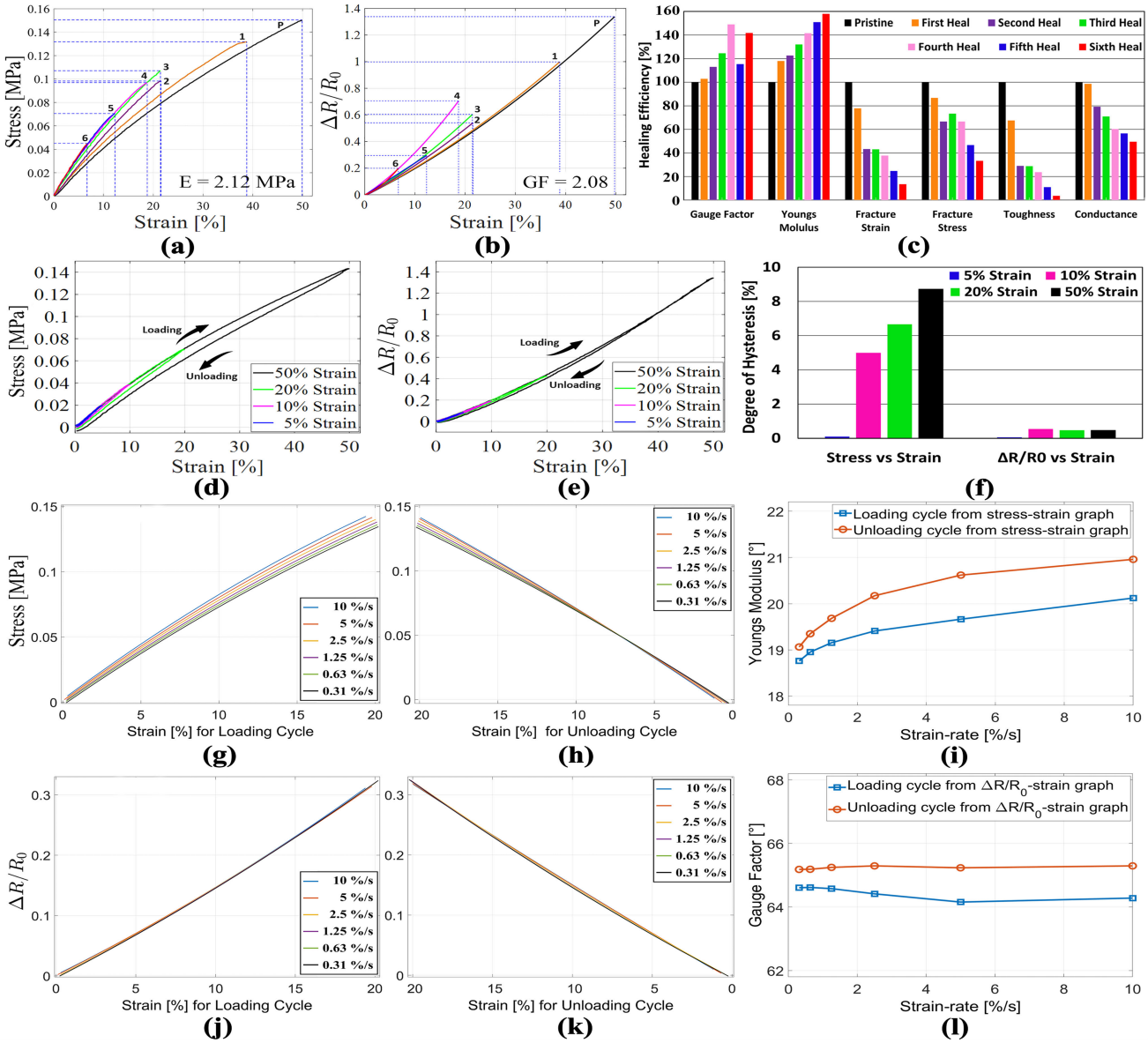

Fig. 4. Third figure in each row is deducted from the analysis of the first two figures of the same row. (a) Stress versus strain for a pristine and multicycle healed sensor across six healing cycles, demonstrating the change in mechanical properties with repeated healing. (b) Change in relative resistance versus strain for the same sensor, illustrating the variation in electrical response through six rupture-healing cycles. (c) Bar graph of the healing efficiency of the sensor generated using (2) for multiple parameters. The graph shows that the GF and Young's modulus (E) increase with increasing healing cycles, whereas fracture strain and stress, toughness, and conductance decrease with increased healing cycles. (d) Mullins cycle for stress versus strain during cyclic loading and unloading with end strain levels of 5%, 10%, 20%, and 50% at a strain rate of 0.17 mm/s showing the DH and the mechanical behavior of the material. (e) Mullins cycle for relative resistance change versus strain under the same conditions, illustrating the electrical hysteresis of the sensor. (f) Bar graph illustrating the DH for material and electrical properties at different strain levels deducted from (d) and (e) calculated using (5). The material DH shows less than 9% at 50% strain, highlighting its viscoelastic behavior. An important finding here is that the electrical DH remains below 1% for all the strain levels and keeps on decreasing with increased strain levels. This demonstrates the sensor's suitability for control applications requiring high-speed feedback. (g) and (h) Stress versus strain at different strain rates for loading and unloading conditions, respectively, showing the material response of the sensor. (i) Line graph of the slope of Young's modulus [arc tan(E)] versus strain rate for both loading and unloading cycles, highlighting the increase in slope with increasing strain rate. (j) and (k) Change in relative resistance versus strain under the same conditions, illustrating the electrical response of the sensor. (l) Line graph of the slope of the GF [arc tan(GF)] versus strain rate, showing the consistent slope across all strain rates for both loading and unloading cycles, indicating that the electrical behavior (change in relative resistance) of the sensor is independent of strain rate.

At the sensory level, conductance (the inverse of resistance) decreases with each successive damage-healing cycle. This can be attributed to two phenomena. First, with each damage event, a small amount of LM is removed from the channel and contaminates the fracture surfaces. Although the cavity volume remains unchanged, the volume of LM decreases, resulting in a slight increase in the resistance. Second, each time the Galinstan is exposed to air, oxidation occurs, further increasing the resistance. Finally, it can be seen that the GF is recovered after healing with a 5% increase which can be attributed to the first phenomena mentioned above. Consequently, it can be concluded that the sensory performance of the sensor is

recovered after damage. Nevertheless, there are some fluctuations in the SH efficiency based on GF, in particular for the fifth cycle. These slight fluctuations can result from the LM oxides generated during rupture, especially considering that the sensor was tested without any prior flexing. To minimize this issue, the sensor should be flexed, pressed, and stretched after healing to break the oxide layer, ensuring a stable proper connection between the two endpoints. The changes in GF across successive healing cycles suggest the need for recalibration methods to achieve high accuracy of the sensor's strain sensing capabilities, as will be discussed in Section IV.

B. Hysteresis Analysis

The strain-sensing behavior of the sensor, particularly its Mullins effect, was further investigated. Therefore, the pristine sensor was subsequently loaded and unloaded between 0% and 5%, 10%, 20%, and 50% strain with a strain rate of 0.25%/s. Fig. 4(d) and (e) shows the Mullins cycle for both the stress and change in relative resistance as a function of strain, respectively. This experiment allows calculating the degree of hysteresis (DH) [2], which is calculated as the area within the loop of the loading-unloading cycle, divided by the area under the loading curve, using (5). DH is expressed in percentage

$$\mathbf{DH} = \frac{\left|\int_0^{\epsilon} Z d\epsilon(\mathbf{loading}) - \int_0^{\epsilon} Z d\epsilon(\mathbf{unloading})\right|}{\int_0^{\epsilon} Z d\epsilon(\mathbf{loading})}. \quad (5)$$

The common parameter denoted by the letter "Z" is stress (σ) or change in relative resistance ($\Delta R/R_0$). Using (5), the mechanical (based on stress) and electrical (based on the change in relative resistance) DH was calculated and plotted in Fig. 4(f), for the increasing strain amplitudes of 5%, 10%, 20%, and 50%. These results illustrate a clear hysteresis in the stress–strain behavior, in particular when applying larger strains (e.g., a DH of 9% at 50% strain). This is caused due to the viscoelastic behavior of the substrate material of the sensor. While the DH can vary among different types of elastomers, it is an inherent characteristic of these materials due to their viscoelastic nature. The DA polymers used in this study, have a nonnegligible viscous response in their viscoelastic behavior, which results from dangling chains that are present in the network due to the nonstoichiometric maleimide-to-furan ratio (r), leading to unbound furan ends [47].

When looking at the resistance-versus-strain relationship in Fig. 4(e), it is evident that the relative change in relative resistance is significantly less affected by hysteresis, compared with the hysteresis observed on stress-versus-strain graph [see Fig. 4(d)]. When cycled up to 50% strain, an almost negligible electrical DH of 1% is registered. This is because, in LM-based stretchable sensors, the change in resistance depends on geometrical changes in the conductive channel/circuit, which are almost exclusively influenced by strain rather than stress. Being liquid, the electrical circuit does not experience stress and the resistivity of the LM remains nearly constant. In other words, the LM-based strain sensors work according to the working principle of a strain gauge sensor rather than the piezoresistivity phenomenon. This contrasts sharply with SH piezoresistive sensors made by compounding SH polymers with conductive fillers [15]. Their piezoresistive behavior depends on both geometrical changes and changes in conductivity due to the reorganization of the conductive particles and/or agglomerates during straining. This negligible hysteresis, which is typical for LM-based sensors facilitates the creation of analytical, time-independent sensor models (see Section IV) which can be used in dynamic conditions or by dynamic controllers, e.g., in feedback controllers for soft robots. Consequently, the authors believe that LM-based circuits can be an enabler for SH polymers with nonnegligible viscoelastic properties in SH devices, including smart wearables.

C. Strain-Rate Independence

In the context of analyzing further the time dependency of the SH sensor, its resistance-versus-strain behavior is analyzed for different strain rates, including 0.31%/s, 0.63%/s, 1.25%/s, 2.5%/s, 5%/s, and 10%/s, in a 0% to 20% strain window. Fig. 4(g) and (h), and (j) and (k) shows the stress and change in relative resistance as a function of the strain both in loading and unloading conditions, respectively. Based on these data, the slopes (arc tangent) of the graphs are calculated in units of $^{\circ}$ for both Young's modulus and GF using linear regression. The slope of Young's modulus and GF are plotted as a function of the strain rate, as shown in Fig. 4(i) and (l), respectively. While Young's modulus clearly increases with a higher strain rate, GF remains practically unchanged, during both loading and unloading cycles. This demonstrates that the sensing of the SH sensor is time-independent and solely dependent on the applied strain.

D. Cyclic Testing Up to 800 Cycles

Both the pristine and healed sensors were subjected to a cyclic test using a trapezoidal waveform with a strain amplitude of 20% with a strain rate of 15.6%/s for a total of 800 cycles. The test was performed in ~48 min. Fig. 5(a) and (d) represents the change in relative resistance versus time for the pristine and the healed sensor, respectively. Fig. 5(b), (e), and (c), (f) shows zoomed-in-view images of the first 10 and last 10 cycles, respectively. Fig. 5(g) displays the change in relative resistance versus strain for the pristine and healed sensor.

First of all, in Fig. 5(a), it can be seen that the response of the pristine sensor is very repeatable, even at the end of 800 cycles. This can be quantitatively illustrated by a low drift of less than 5% over a total of 800 cycles, which is relatively low for SH stretchable strain sensors [40]. The drift of the sensor was measured for both the peak (20% strain) and trough (0% strain) values of the trapezoidal waveform and compared to the average peak-to-peak value of the change in relative resistance. More precisely, for the pristine sensor, the drift, standard deviation, and root mean square error (RMSE)measured for the peak were 4.52%, 1.5×10^{-3}, and 1.8×10^{-3}, respectively, and for the trough were 4.79%, 6×10^{-4}, and 3×10^{-4}, respectively. In addition, when looking at Fig. 5(g), where the change in relative resistance is plotted as a function of strain for this cyclic experiment, it is evident that the sensing behavior changes only slightly over a large number of cycles, simplifying sensor modeling.

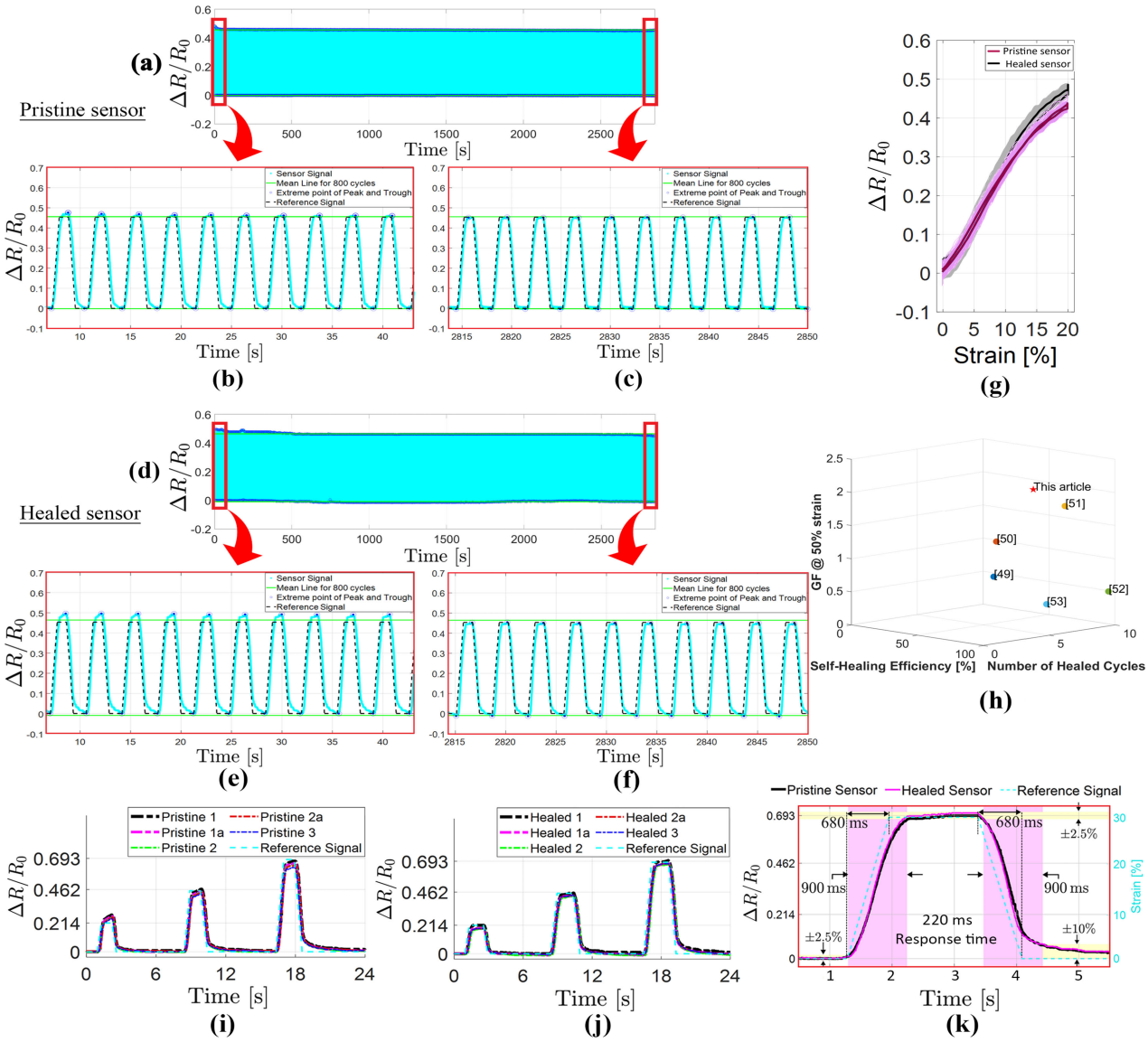

Fig. 5. (a) Change in relative resistance versus time for the pristine sensor over 800 cycles, each lasting 3.56 s. The total duration was 48 min for 20% strain amplitude. The average peak-to-peak value was 0.45 for the pristine sensor. The drift measured was less than 5%. (b) Zoomed-in-view image of the first 10 cycles for the pristine sensor. (c) Zoomed-in-view image of the last 10 cycles for the pristine sensor. (d) Change in relative resistance versus time for the healed sensor over 800 cycles for 20% strain amplitude. The average peak-to-peak value was 0.47 for the healed sensor. The drift measured was less than 10%. (e) Zoomed-in-view image of the first 10 cycles for the healed sensor. (f) Zoomed-in-view image of the last 10 cycles for the healed sensor. (g) Change in relative resistance versus strain graph for the pristine (pink) and the healed (black) sensor. (h) Comparative analysis of SH LM strain sensors, comparing GF at 50% strain, SH performance, and number of healed cycles with recent studies. (i) Repeatability testing results of the pristine sensor under trapezoidal cyclic loading at 10%, 20%, and 30% strain levels, with three samples tested on the first day and two retested after seven days. (j) Repeatability testing results of the healed sensor under the same conditions. (k) Step response test of the pristine and healed sensor at 30% strain amplitude (21 mm) showed both followed the reference strain within 900 ms. The motor applied strain to a 70-mm gauge length in 680 ms. The sensor response time was 220 ms, with maximum errors of 2.5% and 10% for loading and unloading cycles, respectively.

This experiment was repeated on a healed sensor. From Fig. 5(d), it can be concluded that the healed sensor has stable sensing behavior and its electrical properties can be recovered, illustrated by a drift of less than 10%. However, the GF and the peak resistance value slightly changed after healing. The pristine sensor has an average peak-to-peak value of 0.45, and the healed sensor has a slightly higher one of 0.47. More specifically for the healed sensor, the drift, the standard deviation, and the RMSE measured for the peak were 9.64%, 8×10^{-3}, and 5×10^{-2}, respectively, and for the trough were 3.1%, 5×10^{-3}, and 2×10^{-2}, respectively.

The higher drift observed in the healed sensor primarily occurs during the initial phase of the experiment, before the 500-s mark. As shown in Fig. 5(d), the initial portion of the signal exhibits relatively high variability. This can be attributed to the rearrangement of oxidized LM generated at the interface during rupture. At this early stage of the healing process, the connection between the broken LM endpoints is not yet fully stabilized.

However, as the test progresses, the signal becomes stable with minimal drift. This stabilization follows similar reasoning discussed in Section III-A, where it is noted that the sensor must be flexed, pressed, and stretched after healing to break the oxide layer and restore a reliable electrical connection.

This study demonstrates that straightforward, time-independent analytical models, such as a linear model defined by the GF, are adequate for calibrating the sensor for various applications involving cyclic loads. Finally, this study demonstrates that both the pristine and healed sensors fully recovered their sensing abilities, showing minimal drift with no signs of breakage or failure.

E. Repeatability

To evaluate the repeatability of the SH stretchable strain sensor, cyclic loading was applied using a trapezoidal waveform with increasing strain amplitudes of 10%, 20%, and 30%. This test was conducted on both pristine and healed sensors. The repeatability test was conducted on three different samples (1–3) on the first day for both pristine and healed sensors. To assess long-term stability, samples 1a and 2a were retested after seven days following the same protocol.

Fig. 5(i) and (j) illustrates the repeatability results, where the sensor output closely aligns with the reference signal, represented by the actuator's trapezoidal motion. The results confirm the sensor's reliability over time, as samples 1a and 2a maintain similar performance to their initial tests (samples 1 and 2, respectively) even after several days. Furthermore, the response remains consistent across different samples (1–3) for both pristine and healed sensors, demonstrating repeatable behavior. The pristine and healed sensors exhibit high repeatability, with an RMSE of less than 5% when compared with the reference signal.

F. Step Response

A step response test was conducted to analyse the sensor's dynamic response. The pristine and healed sensor was subjected to a single loading and unloading cycle at 30% strain, with a strain rate of 44%/s, as shown in Fig. 5(k). A strain step of 21 mm was applied within 680 ms to a 70-mm gauge length, achieving 30% strain. Both pristine and healed sensors followed the reference strain closely within 900 ms for both extension and relaxation. The response time was calculated as 220 ms, which is suitable for most applications. The extension step had an error of less than 2.5%, while the relaxation step exhibited an error of less than 10% due to material hysteresis. The difference in response time between the pristine and healed sensors was negligible, further confirming their dynamic reliability.

IV. Sensor Model and (Re)Calibration

Due to the time-independence (negligible electrical hysteresis, strain-rate independence, and small drift) of the strain-sensing behavior, an analytical model can be developed to describe the relationship between applied strain and change in relative resistance. Two models were proposed to achieve this mathematical equation, a linear model and a parabolic model. These models are described by the following equations:

$$\epsilon_{\text{Linear Model (\%)}} = \frac{\frac{R-R_0}{R_0}}{\text{GF}} \times 100 \tag{6}$$

$$\epsilon_{\text{Parabolic Model (\%)}} = \frac{-v \pm \sqrt{v^2 - 4u\left(-\frac{R-R_0}{R_0}\right)}}{2u} \tag{7}$$

where R_0 is the initial resistance at rest, R is the resistance measured during straining of the sensor, and GF is the gauge factor, which are the parameters of the linear model, and u and v are the parameters of the parabolic model. To develop robust models, the sensor was exposed to a complex strain profile. This involved a trapezoidal waveform with progressively increasing strain amplitudes of 10%, 20%, and 30%, as illustrated in Fig. 6(a). Throughout the process, the resistance was monitored. Based on this experimental data of the pristine sensor, both models were fit using ordinary least square (OLS) regression. This resulted in the parameters, which are presented in Table I together with RMSE.

Based on the low-RMSE values (<5%) for the (re-)calibrated models, it is clear that a very good fit can be achieved in both cases. As illustrated in Fig. 6(b), both models for pristine and healed sensors show a good fit in the 0%–30% strain window. This is emphasized, as shown in Fig. 6(a), step 1, which shows that the applied strain coincides very well with the measured strain for both the linear and parabolic model of the pristine sensor. Although relatively small, some errors are visible during the relaxation (unloading) step in the zoomed-in-view images, due to the viscoelastic behavior of the encapsulant. Nevertheless, the sensing behavior is very linear. Indicating that for low-strain applications, below 30% the linear model based on GF is more than sufficient. At higher strains, the curve starts to deviate from linear behavior, illustrating the need for a higher order model, such as the parabolic model. Consequently, for the complex trapezoidal waveform, which strains up to 30%, the parabolic model has a marginally lower RMSE value.

Fig. 6(a), step 2, illustrates the performance of the sensor after being cut in half and healed at 60 °C for 4 h. When using the model derived from the pristine sensor, e.g., without performing any recalibration. It is clear that a large part of the sensor performance is recovered, making it feasible to use the sensor without recalibration. Due to partial healing, an alteration is seen in both the initial resistance and the resistance–strain relationship, leading to a baseline shift visible as an offset in the zoomed-in-view images in Fig. 6(a), step 2, and an increase in RMSE value, as shown in Table I. A practical method for recalibration involves a simple R_0 recalibration, which relies solely on measuring the initial resistance of the sensor in unloaded conditions after healing. This approach recalibrates the sensor without requiring movement, making it useful in real-world applications. As shown in Fig. 6(a), step 3, and the lower RMSE value in Table I, this leads to an improved fitting. Finally, to increase the sensory recovery, a full calibration can be performed on the healed sensor, refitting the linear or parabolic model. This results in fitting

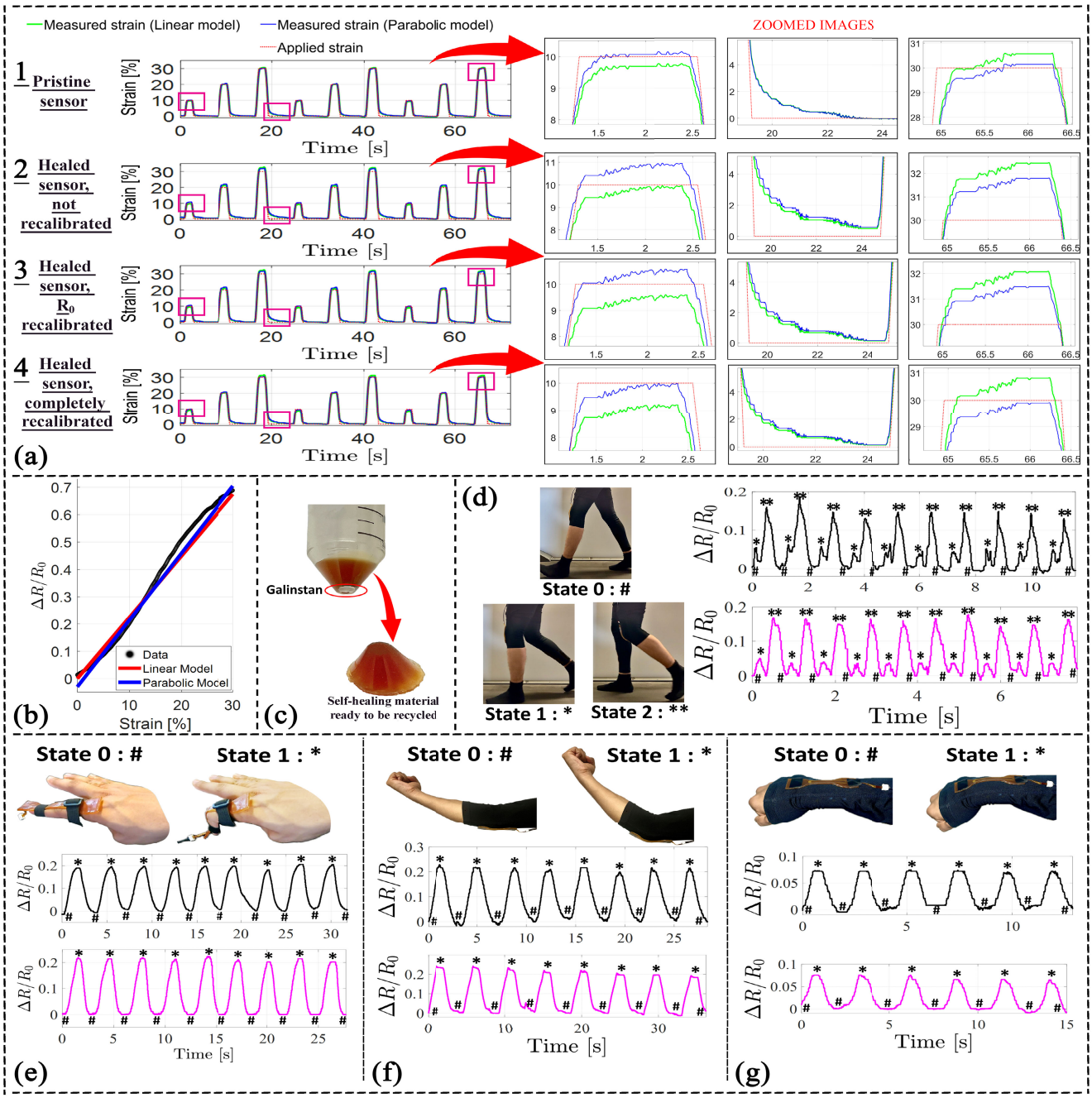

Fig. 6. (a) Sensors' performance by applying trapezoid strain signal with fluctuating amplitude, and comparing the applied strain signal with that of the measured strain signal, which was reconstructed utilizing the linear and parabolic model. Step 1: results of a pristine sensor in which the parameters of the linear and parabolic model were derived using ordinary least squares regression, leading to RMSE values of 4.5% and 4%, respectively. Step: 2 results of a healed sensor with the same pristine model, exhibiting higher RMSE values of 6% and 6.5% for the linear and parabolic models, respectively, indicating the need for recalibration. Step 3: results of a sensor where the linear and parabolic model was recalibrated model solely based on the change in initial resistance (R_0) (baseline resistance). This leads to reduced RMSE values of 5.5% and 5%, respectively. Step 4: results of the healed sensor for which a full recalibration was done, e.g., the parameters of the linear and parabolic model were again derived using regression, leading to RMSE values of 5% and 4.5% respectively, just slightly higher than the pristine case. (b) Linear and parabolic model generated using data from the pristine sensor. (c) The sensor substrate, along with Galinstan, was chopped into pieces and placed in a conical tube, which was then heated at 140 °C, well above the gel transition temperature. It was then quickly transferred to a centrifuge, which separated the denser Galinstan to the extremity from the SH material for recycling/reprocessing. Pristine (black graph) and the healed (magenta graph) sensors were integrated into wearables to monitor the movements of the (d) knee, (e) finger, (f) elbow, and (g) wrist, demonstrating consistent performance. The SH ability of the sensor ensures durability in case of damages such as punctures or cross-sectional tears, which is crucial for wearable applications.

and RMSE values comparable to those of the pristine sensor, indicating that the combination of material-based healing and software compensation (recalibration) achieves full recovery of the sensor's performance.

V. Proof of Concept for Separation and Recycling

A significant challenge facing embedded flexible and stretchable sensors is their poor recyclability, exacerbated

TABLE I
CONSTANTS USED AND RMSE VALUES MEASURED FOR VARIOUS PRISTINE AND HEALED SENSORS USING A LINEAR AND PARABOLIC MODEL

	R_0	GF	u $\times 10^{-2}$	v $\times 10^{-2}$	Linear Model		Parabolic Model	
					RMSE	RMSE [%]	RMSE	RMSE [%]
Pristine sensor, completely calibrated	2.7	2.2	0.01	0.23	0.9	4.5	0.8	4
Healed Sensor, not recalibrated	2.7	2.2	0.01	0.23	1.2	6	1.3	6.5
Healed Sensor, R_0 recalibrated	2.8	2.2	0.01	0.23	1.1	5.5	1.0	5
Healed Sensor, completely recalibrated	2.8	2.3	0.01	0.24	1	5	0.9	4.5

by two critical issues. First, many flexible and stretchable substrates, such as silicones and rubbers, cannot undergo reprocessing because their polymer networks are irreversibly crosslinked. Second, achieving separation between conductive channels and the substrate, which is crucial for recycling individual materials, is challenging or even impossible. This article presents a preliminary proof of concept for a separation method involving DA polymers and LMs. The technique utilizes centrifugal force to exploit the reversible solid-to-liquid transition of DA polymers and the density contrast between the LM ($\rho = 6.44$ g/cm^3) and the polymer ($\rho = 1.17$ g/cm^3).

While many reversible polymers undergo degelation at elevated temperatures, resulting from extensive bond breaking, DA polymers exhibit notably low viscosities in their liquid phase, particularly well above their gelation temperature (T_{gel}). This is also the case for DPBM-FT5000-r0.5, which exhibits viscosities as low as 0.1 Pa ·s at 140 °C, well above their T_{gel} of 80 °C [28].

First, the flex PCB was mechanically removed (e.g., cut using a blade). Next the sensor was cut into 5 × 5 × 3 mm^3 parts, which were placed in a conical tube. The tube is subsequently heated in an oven set at 140 °C, leading to the degelation of the DA polymer into a low-viscosity liquid polymer. Once liquefied, the tube was promptly transferred to a centrifuge and centrifuged for 10 min at 5000 r/min. The high centrifugal force generated during this process causes the denser LM to separate out toward the extremity of the tube, as shown in Fig. 6(c). After centrifugation, the materials were cooled down, leading to the solidification of the DA polymer due to recrosslinking. Upon being solid, the DA polymer could be easily removed from Galinstan LM. This method efficiently recycles the SH substrate, facilitating reprocessing, minimizing waste, and promoting sustainability.

VI. PRISTINE AND HEALED SENSOR FOR HUMAN MOTION MONITORING

The strain sensor produced demonstrates a fracture strain of approximately 50%, which is sufficient for a wide range of smart wearable applications. Most human motion monitoring tasks occur within a strain range of 0%–50%, and commonly between 0% and 30% [38], [45]. For instance, strain sensors used in artificial sound detection (e.g., detecting throat vibrations during speech by placing the sensor on Adam's apple), carotid pulse and eye-blink monitoring, and finger bending typically operate within this range [45]. The encapsulating material of the sensor produced itself exhibits a higher fracture strain (240%) at the material level [28]. However, the reduced stretchability at the application level is primarily attributed to fabrication-related limitations such as air bubbles and particulate contamination encountered during upscaling (115-mm length). These challenges may be addressed in future studies through process optimization and improved manufacturing control.

To validate the SH stretchable strain sensor in applications, both pristine and healed sensors were integrated into a wearable fabric to monitor various human motions, specifically targeting movements of the fingers, wrist, elbow, and knee. Fig. 6(d)–(g) illustrates the change in resistance ($\Delta R/R_0$) over time for both pristine and healed sensors, where the black lines represent motion from the pristine sensor and the magenta lines represent motion from the healed sensor. Fig. 6(d) shows a person walking on a treadmill, with sensors attached to the knee (patella bone) region. Walking involves a cyclic repetition of the gait cycle, which includes distinct peaks at various states. In normal walking, the gait cycle has two peaks: "state 1" (the first peak) and "state 2" (the second peak). "State 0," known as "heel strike," occurs when the knee angle is close to 0°. "State 1," the "loading response," features a short amplitude peak followed by a decrease in knee angle during "mid-stance." A high peak at "state 2," known as "toe-off," corresponds to the highest knee angle in the gait cycle. The pristine and healed sensors display consistent peaks corresponding to each step in the gait cycle. Fig. 6(e) and (f) depicts the sensor aligned to the index finger and elbow, respectively, for bending and straightening motions. For the finger, "state 0" represents the straightened position, where the resistance is at its lowest peak, and "state 1" represents the fully bent position, where the resistance reaches its highest peak. Similarly, for the elbow, "state 0" corresponds to the straightened position with the lowest resistance peak, and "state 1" corresponds to the fully bent position with the highest resistance peak. The pristine sensor shows a regular pattern of resistance change corresponding to the finger and elbow movements. The healed sensor, exhibiting a similar shape to the pristine sensor, closely follows the bending and straightening motions, indicating its ability to accurately track these movements even after healing. Fig. 6(g) shows the sensor attached to the wrist for flexion and extension movements. Flexion of the wrist involves bending it so that the palm moves toward the forearm, reaching the highest resistance change, referred to as "state 1." Extension involves straightening the wrist or bending it backwards, reaching the lowest resistance change, known as "state 0." The pristine and healed sensors display consistent resistance patterns corresponding to these movements. The healed sensor's response closely follows the pattern of the pristine sensor, indicating that the sensor retains its functionality even after healing. The integration of these SH sensors significantly enhances the durability and longevity

of wearable sensors, particularly in the face of damage or tears. Despite minor amplitude differences between the pristine and healed sensors posthealing due to an increase in GF, the healed sensors demonstrate remarkable recovery capabilities, ensuring accurate motion monitoring. Graphs Fig. 6(d)–(g) consistently illustrate clear, distinct resistance changes in the pristine sensor corresponding to various human motions. These findings validate the efficacy of SH sensors in applications related to human motion monitoring. The ability of these sensors to self-heal and maintain performance is especially valuable in wearable technology, where sensors are frequently exposed to large mechanical stress and sharp objects, both potentially induce damage.

VII. Conclusion

This study demonstrated the promise of pairing DA polymers with LM to develop SH stretchable strain sensors for durable and reliable smart wearables. The sensor's ability to recover from electrical and mechanical functionalities after multiple damage cycles represents a significant advancement in sensor technology. In addition, initial progress was made toward enhancing the sustainability of the sensor by demonstrating the recyclability of the material. The innovative approach to sensor design and manufacturing outlined in this article lays the foundation for future developments in SH stretchable electronics, enabling the creation of robust sensors with intricate shapes, precise geometries, and more sustainable, long-lasting smart devices.

The intrinsic SH ability of the DA encapsulant, based on reversible crosslinks, was seamlessly integrated with the Galinstan circuit, which inherently self-healed due to its liquid nature. The SH capability of this new stretchable strain sensor was demonstrated through tests, where it successfully repaired itself from extensive damage after being completely cut into two halves, fully recovering within 4 h at 60 °C. These tests showed that while the mechanical strength of the sensor was only partially restored (with a SH efficiency of 85%), the critical elastic and sensing behaviors within this strain range were effectively recovered, ensuring reliable measurement performance despite minor variations. This healing was robust and reliable, as illustrated by a healed sensor that withstood cyclic loading with a strain amplitude of 20% over 800 cycles. With each damage-healing cycle, the sensor's strength diminished, as demonstrated by six consecutive damage-healing cycles at the same location, most likely due to Galinstan contamination on the fracture surfaces. However, its elastic and sensory behavior continued to be restored. A study by Legrand et al. [43] demonstrated that a controlled manufacturing approach allowed for 63 damage-healing cycles using the DPBM-FT5000-r0.5 DA polymer, highlighting the potential for further optimization in SH systems.

In stark contrast to state-of-the-art polymer-based SH sensors that exploit piezoresistivity, the LM-based SH sensor exhibited superior sensing quality being predominantly strain gauge driven, which is characterized by negligible hysteresis (<1%), strain-rate independence, fast response times (220 ms), and minimal drift (5% over 800 cycles). This stemmed from the liquid nature of the embedded Galinstan circuit, where resistance changes were predominantly driven by strain-induced changes in geometry. The time-independence nature of the LM-based stretchable sensor enabled modeling and calibration using relatively simple analytic models. In the case of polymer-based SH circuits, the piezoresistive behavior depended on both geometrical changes and changes in conductivity due to the reorganization of the conductive particles and/or agglomerates during straining, resulting in undesired time-dependent effects such as large hysteresis. As such, determining analytical or numerical models for these is very challenging, if not impossible.

Consequently, both linear and parabolic models were used to fit the strain-sensing behavior of the pristine and healed sensors. Low RMSE values indicated that these models provided excellent fits, even for complex trapezoidal waveforms with increasing strain amplitudes, demonstrating the sensor's stability and reliability. Although the sensing performance was effectively recovered after healing, there was a slight decrease in accuracy due to changes in baseline resistance and resistance–strain relationship. Future work could investigate the recovery of the sensing performance after SH using more complex models to gain a deeper understanding. Nevertheless, this article showed that recalibrating the baseline resistance or performing a full recalibration significantly improved or even completely restored the sensing performance. This highlights the advantage of combining material-based SH with software-based adaptation, such as recalibration.

To contextualize our findings within the broader landscape of LM-based SH strain sensors, a comparative analysis was conducted against representative recent studies [as summarized in Fig. 5(h)] [48], [49], [50], [51], [52]. Compared with these reports, the sensor presented in this work exhibits a superior GF (=2.4 at 50% strain), reflecting enhanced sensitivity to small deformations. Our sensor also demonstrates comparable SH performance (80% healing efficiency and 6 healed cycles), while maintaining structural integrity without delamination issues. [49], [50], [52] report higher SH efficiencies; however, they exhibit lower GFs and fewer healed cycles in comparison. [51] presents a slightly lower GF but demonstrates a marginally higher number of healed cycles and SH efficiency. Meanwhile, Sun et al. [48] exhibited strong healing performance (95%) and the highest number of healed cycles (10), but it has one of the lowest GFs, indicating reduced sensitivity. This highlights the balanced and robust performance of our sensor in terms of sensitivity, healing repeatability, and efficiency. Furthermore, our sensor uniquely combines strain-independent behavior, negligible hysteresis (<1%), and minimal drift for the pristine sensor (<5%), all of which are critical for reliable and repeatable sensing. Notably, while drift characteristics of healed sensors are rarely reported in the literature, our work demonstrates that the healed sensor also maintains low drift (<10%), underscoring its long-term reliability. Importantly, this work introduces a step toward recyclable sensor architecture by leveraging a reprocessable DA polymer matrix and a LM circuit—an ecological aspect rarely addressed in existing literature. These features collectively position our sensor as a robust and forward-looking solution in the evolving field of SH stretchable electronics.

A proof of concept was developed to demonstrate that the SH sensor can be recycled through a unique recycling procedure—an ecological aspect rarely addressed in existing literature. This process, enabled by centrifugal separation of the reprocessable substrate and the LM, represents an initial step toward benchmarking recyclability in SH-based strain sensors. This technique leveraged the reversible solid-liquid transition of DA polymers, their remarkably low viscosity in their liquid state, and the high density of Galinstan. Typical stretchable sensors use substrates that are permanently cross-linked and therefore irreversible, hence being a nonrecyclable sensor. In contrast, sensors made with DA polymers and LMs show strong potential for complete recyclability and ecological sustainability.

Finally, the practical application of the SH stretchable strain sensor was demonstrated by embedding it in wearable fabrics capable of effectively monitoring various human movements, including finger, wrist, elbow, and knee bending, for both pristine and healed sensors. This highlighted its potential applications in areas like healthcare monitoring, soft robotics, and biomedical engineering. Due to its combination of stretchability, durability, reliability, SH capability, and recyclability, this sensor stood out as a promising technology for advancing smart wearables and textiles, flexible electronics, soft robotics, and various other fields beyond.

Acknowledgment

Rathul Nengminza Sangma, Kevin Langlois, Ehsan Mirabdollah, and Bram Vanderborght are with BruBotics, Vrije Universiteit Brussel and imec, 1050 Ixelles, Belgium (e-mail: rathul.nengminza.sangma@vub.be).

Seppe Terryn is with BruBotics, Vrije Universiteit Brussel and imec, 1050 Ixelles, Belgium, and also with the Department of Materials and Chemistry, Sustainable Materials Engineering, Vrije Universiteit Brussel, 1050 Ixelles, Belgium.

Maximilian Krack, Lennert Purnal, Michael Daenen, and Wim Deferme are with the Institute for Materials Research, Hasselt University, 3590 Diepenbeek, Belgium.

Fatemeh Sahraeeazartamar, Parth Vinayakrao Sewlikar, Iris De Graeve, Joost Brancart, and Guy Van Assche are with the Department of Materials and Chemistry, Sustainable Materials Engineering, Vrije Universiteit Brussel, 1050 Ixelles, Belgium.

Declaration of Competing Interest

The authors declare that they do not have any conflict of interest that could have potentially influenced the findings presented in this document.

Data Availability

Data will be made available on request.

References

[1] Z. Shen et al., "Progress of flexible strain sensors for physiological signal monitoring," *Biosensors Bioelectron.*, vol. 211, Sep. 2022, Art. no. 114298.

[2] Y. Luo et al., "Flexible liquid metal-based microfluidic strain sensors with fractal-designed microchannels for monitoring human motion and physiological signals," *Biosensors Bioelectron.*, vol. 246, Feb. 2024, Art. no. 115905.

[3] M. Jose, G. Oudebrouckx, S. Bormans, P. Veske, R. Thoelen, and W. Deferme, "Monitoring body fluids in textiles: Combining impedance and thermal principles in a printed, wearable, and washable sensor," *ACS Sensors*, vol. 6, no. 3, pp. 896–907, Mar. 2021.

[4] G. Bugmann, M. Siegel, and R. Burcin, "A role for robotics in sustainable development?" in *Proc. IEEE Africon*, Sep. 2011, pp. 1–4.

[5] K. Munirathinam, J. Park, Y.-J. Jeong, and D.-W. Lee, "Galinstan-based flexible microfluidic device for wireless human-sensor applications," *Sens. Actuators A, Phys.*, vol. 315, Nov. 2020, Art. no. 112344.

[6] E. Roels et al., "Processing of self-healing polymers for soft robotics," *Adv. Mater.*, vol. 34, no. 1, Oct. 2021, Art. no. 2104798.

[7] Z. Wang, L. Sun, Y. Ni, L. Liu, and W. Xu, "Flexible electronics and healthcare applications," *Frontiers Nanotechnol.*, vol. 3, Mar. 2021, Art. no. 625989.

[8] W. Hou, Q. Liao, S. Xie, Y. Song, and L. Qin, "Prospects and challenges of flexible stretchable electrodes for electronics," *Coatings*, vol. 12, no. 5, p. 558, Apr. 2022.

[9] J. Yoo, S. Li, D.-H. Kim, J. Yang, and M. K. Choi, "Materials and design strategies for stretchable electroluminescent devices," *Nanosc. Horizons*, vol. 7, no. 8, pp. 801–821, 2022.

[10] S. Huang, Y. Liu, Y. Zhao, Z. Ren, and C. F. Guo, "Flexible electronics: Stretchable electrodes and their future," *Adv. Funct. Mater.*, vol. 29, no. 6, Feb. 2019, Art. no. 1805924.

[11] K. Liu, B. Ouyang, X. Guo, Y. Guo, and Y. Liu, "Advances in flexible organic field-effect transistors and their applications for flexible electronics," *Npj Flexible Electron.*, vol. 6, no. 1, p. 1, Jan. 2022.

[12] D. Zhang, T. Huang, and L. Duan, "Emerging self-emissive technologies for flexible displays," *Adv. Mater.*, vol. 32, no. 15, Apr. 2020, Art. no. 1902391.

[13] Y. Chi, Y. Li, Y. Zhao, Y. Hong, Y. Tang, and J. Yin, "Bistable and multistable actuators for soft robots: Structures, materials, and functionalities," *Adv. Mater.*, vol. 34, no. 19, May 2022, Art. no. 2110384.

[14] Y.-S. Guan et al., "Air/water interfacial assembled rubbery semiconducting nanofilm for fully rubbery integrated electronics," *Sci. Adv.*, vol. 6, no. 38, p. 3656, Sep. 2020.

[15] E. Roels et al., "Self-healing sensorized soft robots," *Mater. Today Electron.*, vol. 1, May 2022, Art. no. 100003.

[16] K. Zhao, Y. Wang, J. Guo, S. Zhang, and W. Niu, "Photonic vitrimer-based electronics with self-healing and ultrastable visual-digital outputs for wireless strain sensing," *Chem. Eng. J.*, vol. 450, Dec. 2022, Art. no. 138285.

[17] T. Haidegger et al., "Robotics: Enabler and inhibitor of the sustainable development goals," *Sustain. Prod. Consumption*, vol. 43, pp. 422–434, Dec. 2023.

[18] G. Scandurra, A. Arena, and C. Ciofi, "A brief review on flexible electronics for IoT: Solutions for sustainability and new perspectives for designers," *Sensors*, vol. 23, no. 11, p. 5264, Jun. 2023.

[19] B. Kılıçarslan, I. Bozyel, D. Gökcen, and C. Bayram, "Sustainable macromolecular materials in flexible electronics," *Macromolecular Mater. Eng.*, vol. 307, no. 6, Jun. 2022, Art. no. 2100978.

[20] M. D. Dickey, "Stretchable and soft electronics using liquid metals," *Adv. Mater.*, vol. 29, no. 27, Jul. 2017, Art. no. 1606425.

[21] S. Kim, B. Yoo, M. Miller, D. Bowen, D. J. Pines, and K. M. Daniels, "EGaIn-Silicone-based highly stretchable and flexible strain sensor for real-time two joint robotic motion monitoring," *Sens. Actuators A, Phys.*, vol. 342, Aug. 2022, Art. no. 113659. [Online]. Available: https://www.sciencedirect.com/science/article/pii/S0924424722002977

[22] S. Terryn et al., "A review on self-healing polymers for soft robotics," *Mater. Today*, vol. 47, pp. 187–205, May 2021. [Online]. Available: https://www.sciencedirect.com/science/article/pii/S1369702121000080

[23] A. Cuvellier, R. Verhelle, J. Brancart, B. Vanderborght, G. Van Assche, and H. Rahier, "The influence of stereochemistry on the reactivity of the Diels–Alder cycloaddition and the implications for reversible network polymerization," *Polym. Chem.*, vol. 10, no. 4, pp. 473–485, 2019.

[24] S. Terryn et al., "Structure—Property relationships of self-healing polymer networks based on reversible Diels–Alder chemistry," *Macromolecules*, vol. 55, no. 13, pp. 5497–5513, Jun. 2022.

[25] F. Sahraeeazartamar et al., "Effect of secondary particles on self-healing and electromechanical properties of polymer composites based on carbon black and a Diels–Alder network," *ACS Appl. Polym. Mater.*, vol. 5, no. 10, pp. 7813–7830, Sep. 2023.

[26] F. Sahraeeazartamar et al., "Designing flexible and self-healing electronics using hybrid carbon black/nanoclay composites based on Diels–Alder dynamic covalent networks," *Macromolecules*, vol. 57, no. 2, pp. 539–553, Jan. 2024.

[27] S. Terryn, J. Brancart, D. Lefeber, G. Van Assche, and B. Vanderborght, "Self-healing soft pneumatic robots," *Sci. Robot.*, vol. 2, no. 9, Aug. 2017, Art. no. eaan4268.

[28] A. Safaei et al., "Fast self-healing at room temperature in Diels–Alder elastomers," *Polymers*, vol. 15, no. 17, p. 3527, 2023.
[29] E. Roels, S. Terryn, J. Brancart, G. Van Assche, and B. Vanderborght, "A multi-material self-healing soft gripper," in *Proc. IEEE Int. Conf. Soft. Robot.*, May 2019, pp. 316–321.
[30] S. Terryn, E. Roels, J. Brancart, G. Van Assche, and B. Vanderborght, "Self-healing and high interfacial strength in multi-material soft pneumatic robots via reversible Diels–Alder bonds," *Actuators*, vol. 9, no. 2, p. 34, Apr. 2020.
[31] A. Mehmood et al., "Graphene based nanomaterials for strain sensor application—A review," *J. Environ. Chem. Eng.*, vol. 8, no. 3, Jun. 2020, Art. no. 103743.
[32] S. Terryn, D. Hardman, T. G. Thuruthel, E. Roels, F. Sahraeeazartamar, and F. Iida, "Learning-based damage recovery for healable soft electronic skins," *Adv. Intell. Syst.*, vol. 4, no. 12, Dec. 2022, Art. no. 2200115.
[33] M. Baharfar and K. Kalantar-Zadeh, "Emerging role of liquid metals in sensing," *ACS Sensors*, vol. 7, no. 2, pp. 386–408, Feb. 2022.
[34] U. Daalkhaijav, O. D. Yirmibesoglu, S. Walker, and Y. Mengüç, "Rheological modification of liquid metal for additive manufacturing of stretchable electronics," *Adv. Mater. Technol.*, vol. 3, no. 4, Apr. 2018, Art. no. 1700351.
[35] X. Wang et al., "Biocompatible liquid metal coated stretchable electrospinning film for strain sensors monitoring system," *Sci. China Mater.*, vol. 65, no. 8, pp. 2235–2243, Aug. 2022.
[36] M. D. Dickey, "Emerging applications of liquid metals featuring surface oxides," *ACS Appl. Mater. Interfaces*, vol. 6, no. 21, pp. 18369–18379, Nov. 2014.
[37] Y.-G. Park, H. S. An, J.-Y. Kim, and J.-U. Park, "High-resolution, reconfigurable printing of liquid metals with three-dimensional structures," *Sci. Adv.*, vol. 5, no. 6, Jun. 2019, Art. no. eaaw2844.
[38] J. Chen et al., "Superelastic, sensitive, and low hysteresis flexible strain sensor based on wave-patterned liquid metal for human activity monitoring," *ACS Appl. Mater. Interfaces*, vol. 12, no. 19, pp. 22200–22211, May 2020.
[39] Y. Plevachuk, V. Sklyarchuk, S. Eckert, G. Gerbeth, and R. Novaković, "Thermophysical properties of the liquid Ga-In-Sn eutectic alloy," *J. Chem. Eng. Data*, vol. 59, no. 3, pp. 757–763, Feb. 2014.
[40] A. Georgopoulou et al., "Soft self-healing resistive-based sensors inspired by sensory transduction in biological systems," *Appl. Mater. Today*, vol. 29, Dec. 2022, Art. no. 101638.
[41] StrategicElements. (2019). *Galinstan Alloy*. [Online]. Available: https://www.strategic-elements.com/produkte/galinstan-1/
[42] S. Nagels, T. Vandenryt, and W. Deferme, "Interconnect, an electronic assembly and a method for manufacturing an electronic assembly," U.S. Patent 11,856,692, Dec. 26, 2023.
[43] J. Legrand, A. Abdulali, D. Hardman, S. Terryn, B. Vanderborght, and F. Iida, "Autonomous testing of the repeatable healability of pneumatic self-healing soft actuators," *Robot. Rep.*, vol. 1, no. 1, pp. 31–41, Sep. 2023.
[44] L. He, J. Shi, B. Tian, H. Zhu, and W. Wu, "Self-healing materials for flexible and stretchable electronics," *Mater. Today Phys.*, vol. 44, May 2024, Art. no. 101448.
[45] S. Ko, A. Chhetry, D. Kim, H. Yoon, and J. Y. Park, "Hysteresis-free double-network hydrogel-based strain sensor for wearable smart bioelectronics," *ACS Appl. Mater. Interfaces*, vol. 14, no. 27, pp. 31363–31372, Jul. 2022.
[46] M. Amjadi, K.-U. Kyung, I. Park, and M. Sitti, "Stretchable, skin-mountable, and wearable strain sensors and their potential applications: A review," *Adv. Funct. Mater.*, vol. 26, no. 11, pp. 1678–1698, Mar. 2016.
[47] A. Safaei, S. Terryn, B. Vanderborght, G. Van Assche, and J. Brancart, "The influence of the furan and maleimide stoichiometry on the thermoreversible Diels–Alder network polymerization," *Polymers*, vol. 13, no. 15, p. 2522, Jul. 2021.
[48] F. Sun et al., "Vascular smooth muscle-inspired architecture enables soft yet tough self-healing materials for durable capacitive strain-sensor," *Nature Commun.*, vol. 14, no. 1, p. 130, Jan. 2023.
[49] J. Xu et al., "Polymerization of moldable self-healing hydrogel with liquid metal nanodroplets for flexible strain-sensing devices," *Chem. Eng. J.*, vol. 392, Jul. 2020, Art. no. 123788.
[50] S. Wu et al., "Highly sensitive and self-healing conductive hydrogels fabricated from cationic cellulose nanofiber-dispersed liquid metal for strain sensors," *Sci. China Mater.*, vol. 66, no. 5, pp. 1923–1933, Jan. 2023.
[51] J. W. Kim, S. Kim, J. Lee, Y. Kim, and J. S. Ha, "A magnetically self-aligning, fast full-device self-healing, skin-attachable liquid metal strain sensor based on photothermal polyurethane," *Adv. Funct. Mater.*, vol. 35, no. 3, Jan. 2025, Art. no. 2411786.
[52] T. Yu, X. Lü, C. Xue, and W. Bao, "Biomimetic three-dimensional microchannel non-destructive self-healing flexible strain sensor based on liquid metal-polydimethylsiloxane elastomer," *Chem. Eng. J.*, vol. 497, Oct. 2024, Art. no. 154526.

Rathul Nengminza Sangma received the bachelor's degree in mechanical engineering from Savitribai Phule Pune University (SPPU), Pune, India, in 2017, and the master's (Hons.) degree in electromechanical engineering from Vrije Universiteit Brussel (VUB), Ixelles, Belgium, in 2022, majoring in mechatronics.

Since then, he has been a Ph.D. Researcher with BruBotics, VUB, affiliated with the Interuniversity Microelectronics Institute (imec), Ixelles, focusing on the characterization of wearable sensors for monitoring human motion and muscle activity.

Seppe Terryn received the M.Sc. degree from Vrije Universiteit Brussel (VUB), Ixelles, Belgium, in 2014.

During his Ph.D. degree, he combined smart materials and robotics, pioneering the multidisciplinary field of "self-healing soft robots." His primary expertise lies in designing multifunctional materials, including self-healing polymers, for advanced (re)processing and (de)manufacturing, as well as for new embodied intelligence and sustainability principles in smart devices like (flexible) electronics and (soft) robotics. His research was supported by Fonds Wetenschappelijk Onderzoek (FWO) Ph.D., junior, and senior postdoctoral grants. Since 2024, he has been an Associate Professor with VUB, leading Ph.D.s and postdoctoral researchers in projects like EU FET SHERO, MSCA ITN SMART, and EIC Transition SHINTO.

Maximilian Krack received the bachelor's and master's degrees in MEMS engineering from the University of Applied Sciences Kaiserslautern, Kaiserslautern, Germany, in 2021 and 2022, respectively.

He started his academic career at the University of Applied Science Kaiserslautern, Kaiserslautern, Germany, in 2017. In 2023, he secured a prestigious personal four-year Ph.D. Scholarship [Fonds Wetenschappelijk Onderzoek (FWO)] focusing on liquid metal deposition for stretchable electronics. Particularly, he is investigating 3-D-printing and spray deposition technologies.

Kevin Langlois, photograph and biography not available at the time of publication.

Fatemeh Sahraeeazartamar received the bachelor's and master's degrees in polymer engineering from Tehran Polytechnic (AUT), Tehran, Iran, in 2015 and 2018, respectively. She pursued her Ph.D. degree with the Physical Chemistry and Polymer Science (FYSC) Research Group, Vrije Universiteit Brussel (VUB), Ixelles, Belgium, in 2024.

During her master's degree, she studied self-healing composites and blends with optimized properties based on Diels–Alder chemistry with a focus on developing sustainable polymers suitable for deformation and damage sensing applications in soft robotics. By investigating these polymers offering opportunities for self-healing behavior she contributed to fabrication of more durable electronic devices such as self-healing stretchable sensors that can autonomously repair damage and maintain their functionality over time to not only enhances the reliability of devices but also extends their operational life, making them ideal for applications requiring flexibility, resilience, continuous performance, and sustainability.

Ehsan Mirabdollah received the bachelor's degree in mechanical engineering from the Sharif University of Technology, Tehran, Iran, in 2016, the master's degree in energy systems engineering and environment from the University of Tehran, Tehran, in 2019, and the master's degree in electromechanical engineering from Vrije Universiteit Brussel (VUB), Ixelles, Belgium, in 2024.

During this time, he co-founded and managed a company specializing in product design and development, with a focus on additive manufacturing from 2016 to 2022. He is currently a Ph.D. candidate at VUB, whose research is funded by Fonds Wetenschappelijk Onderzoek Vlaanderen (FWO). His research focuses on self-healing electronic circuits and sensors, product development, additive manufacturing, and sustainable energy systems.

Lennert Purnal, photograph and biography not available at the time of publication.

Parth Vinayakrao Sewlikar received the M.Sc. degree in materials science and engineering from the Technical University of Delft, Delft, The Netherlands, in 2022. He is currently pursuing the Ph.D. degree with Vrije Universiteit Brussel, Ixelles, Belgium.

As a graduate student, he worked in corrosion prevention of aerospace materials. His key interest lies in understanding the physics and chemistry of materials and its application in emerging technologies. His research focuses on understanding the chemistry of liquid metals, studying the surface and interfaces by material characterization techniques, and developing solutions for enhancing the durability of flexible and stretchable electronic devices.

Iris De Graeve, photograph and biography not available at the time of publication.

Michael Daenen, photograph and biography not available at the time of publication.

Joost Brancart received the Ph.D. degree from Vrije Universiteit Brussel, Ixelles, Belgium, in 2017, on the topic of stimuli-responsive materials for self-healing applications.

He is a Senior Postdoctoral Fellow (FWO) and an Assistant Research Professor with the Sustainable Materials Engineering research group. He specializes in studying the structure-processing-property relations of advanced functional materials, such as dynamic polymer networks, hybrid composites, and blends. He exploits these relations for optimizing the properties and performance of challenging applications, including robotics and flexible electronics. He devotes a lot of research effort on improving the sustainability of polymeric materials at all phases at the lifecycle, from renewable resources over greener synthesis and production processes toward lifetime extension and more sustainable end-of-life scenarios.

Guy Van Assche is an Associate Professor with the Sustainable Materials Engineering research group, Vrije Universiteit Brussel (VUB), Ixelles, Belgium. His research is dedicated to exploring the thermodynamics and kinetics of reactions and transformations within polymer systems. This includes both the development and utilization of sophisticated thermal analysis techniques for experimental studies and the modeling of these processes to understand their effects on material behavior. Since 2008, his research has been expanding to include self-healing and reprocessable polymer networks. He has collaborated with research Prof. B. Vanderborght's Robotics and Multibody Mechanics Group, VUB, pioneering the field of self-healing soft robotics.

Wim Deferme is a Professor with the Institute of Materials Research (IMO-IMOMEC), Hasselt University, Diepenbeek, Belgium. His research focuses on the fundamentals of printing and coating technology for its application in flexible, stretchable, and organic electronics toward organic light-emitting diodes, printed sensors, and liquid-metal-based stretchable interconnections. He is the Head of the Functional Materials Engineering research group—of one postdoctoral researcher, six Ph.D. students, and one project engineer. The main printing/coating technologies studied are ultrasonic spray coating, screen printing, inkjet printing, and the newly invented spray-on-screen printing.

Bram Vanderborght received the Ph.D. degree from Vrije Universiteit Brussel (VUB), Ixelles, Belgium, in 2007.

He performed research at the JRL Laboratory, AIST, Tsukuba, Japan, and did his postdoctoral research at Italian Institute of Technology, Genoa, Italy. Since 2009, he has been a Professor with VUB. He had an ERC starting grant and coordinates three EU projects on self-healing materials for soft robots. His research interests are human–robot collaboration for applications for health and manufacturing such as exoskeletons, prostheses, social robots, drones, and cobots. He was the Core Lab Manager at Flanders Make, Leuven, Belgium, until 2021 and is affiliated with the Interuniversity Microelectronics Institute (imec), Ixelles, Belgium, as Scientific Collaborator.